PCCP

Molecular p-doping in organic liquid crystalline semiconductor: Influence of the charge transfer complex on the properties of mesophase and bulk charge transport

Journal:	*Physical Chemistry Chemical Physics*
Manuscript ID	CP-ART-05-2019-003076.R1
Article Type:	Paper
Date Submitted by the Author:	17-Jul-2019
Complete List of Authors:	Kondratenko, Kirill; ULCO, Physics Boussoualem, Yahia; ULCO, Physics Singh, Dharmendra Pratap; ULCO, Physics VISVANATHAN, RAYSHAN; University of Colorado Boulder, Materials Science and Engineering Duncan, Alexandra; University of Colorado Boulder, Materials Science and Engineering Clark, Noel; University of Colorado, Department of Physics and FLCMRC Legrand, Christian; ULCO, Physics Daoudi, Abdelylah; ULCO, Physics

Journal Name

ARTICLE TYPE

Cite this: DOI: 10.1039/xxxxxxxxxx

Molecular p-doping in organic liquid crystalline semiconductor: Influence of the charge transfer complex on the properties of mesophase and bulk charge transport†

K. Kondratenko*[a], Y. Boussoualem[a], D.P. Singh[a], R. Visvanathan[b], A. E. Duncan[b], N. A. Clark[b], C. Legrand[a] and A. Daoudi[a]

Received Date
Accepted Date

DOI: 10.1039/xxxxxxxxxx

www.rsc.org/journalname

We explore the molecular nature of doping in organic semiconductor (OSC) by employing a liquid crystalline organic semiconductor based on phenyl naphthalene as a model. The mesophase nature of composites which include charge transfer complex (**CTC**) between the OSC (**8-PNP-O12**) and an electron acceptor (**F_4TCNQ**) has been investigated by means of differential scanning calorimetry, polarized optical microscopy and x-ray scattering. Optical and vibrational spectroscopies allow us to explore the characteristics and the amount of charge transfer for **CTC** and expose some properties which appear only in complexed state. We have found this system to exhibit partial charge transfer, which manifests itself in all the phase states of host **8-PNP-O12**, as well as in solution. Due to the lowering of molecular symmetry as a result of the charge transfer, one of the previously IR-only vibrational bands of nitrile group is found to be now active in Raman spectrum. We have also made an attempt to further investigate the influence of dopant introduction on the bulk hole mobility of **8-PNP-O12**. It is found that the presence of **CTC** promotes the hole transport in Smectic B mesophase, however it seems to have somewhat negative influence in the less ordered Smectic A mesophase. This work is aimed to establish the link between the inevitable change of molecular geometry which occurs on charge transfer with the results obtained by spectroscopic techniques and electronic charge carrier mobility measurements.

1 Introduction

Organic semiconductors (OSCs) are the substances which have an extended π-conjugated core and exhibit bulk electronic transport. The OSCs are believed to enable low cost and larg-area production of devices such as light-emitting diodes, photovoltaics and thin-film transistors[1,2,3]. This field of research exhibits sustaining interest during two last decades, especially with apparition of new high performance materials[4]. However to make these materials truly suitable for manufacturing applications, it is necessary to find ways which allow to improve and tune their properties accordingly[5]. One of the common ways to improve the performance of this class of materials is the process called molecular doping.

Conventional semiconductor industry owes its widespread to the doping of silicon-based semiconducting materials. In relation to organic substances, this process is in certain ways similar to the doping of classical semiconductors, however, this direction of research is still in the state of development. The main goal of this process is to improve electronic transporting properties of the host semiconductor. The bulk conductivity of a material (σ) is represented by $\sigma = \mu ne$; where μ denotes the charge carrier mobility, n stands for number density of available carriers, and e is the elementary charge. It is generally assumed that the introduction of doping impurity to the OSCs results in the increase of the available charge carrier amount[6].

The basic idea behind the molecular doping of organic semiconductors lies in their characteristic trait: instead of classical for inorganic semiconductor notions of conductance and valence bands one has to operate with energy levels of frontier molecular orbitals (MOs) - HOMO and LUMO[7,8]. These energies are highly relevant to the process in scope, since they reflect the molecular nature of the material: the OSC in bulk does not form covalently bound single crystals, but should be regarded as an amorphous

* *Email address:* kirill.kondratenko@univ-littoral.fr (K. Kondratenko)
[a] *Univ. Littoral Côte d'Opale, EA 4476 - UDSMM - Unité de Dynamique et Structure de Matériaux Moléculaires, 59140 Dunkerque, France*
[b] *Department of Physics and Soft Materials Research Center, University of Colorado Boulder, Boulder, CO, USA*
† Electronic Supplementary Information (ESI) available: See DOI: 10.1039/b000000x/

solids in case of polymeric OSCs or polycrystalline structure held together with weak van der Waals interactions[9]. This also explains why early attempts of elemental doping were not successful in yielding stable results due to the dopant diffusion[10]. It is then becomes apparent that in order to introduce a "vacant" hole or electron in the system, it is possible to employ another molecule with suitable frontier orbital energy level (a LUMO deeper than HOMO of the host in case of p-doping) which in turn can inject or withdraw an electron on one of the frontier MOs of the host molecule[5].

P-doping of the classic OSC materials like polythiophenes[11] and pentacene[7,12] has been thoroughly explored by numerous groups: it has been confirmed that introduction of strong electron acceptors like the various substituted derivatives of tetracyanoquinodimethane (TCNQ)[13–15] and other molecules possesing deep LUMO levels[3,16] results in substantial increase of the conductivity (sometimes even of several order magnitude[17]). These results have given rise to the profound interest in the closer inspection of intermolecular charge transfer (which is not a new subject by itself[18]) in application to organic electronics[19–22].

It has been widely demonstrated for doped systems to exhibit an increase of charge carriers density[5,6,11]. However, further consequences of this process are not sufficiently addressed. It is expected that a change in electron arrangement of two neighboring molecules of the donor and acceptor substances may lead to the change in their respective geometry, which may be further expressed as a change in their phase structure on higher scale[23–27]. For the OSCs, the molecular geometry and order are believed to be the ones of the key parameters governing their performance, notably, the charge carrier mobility[28].

One of the ways to explore the influence of the doping on these parameters is to utilize an OSC which order can be effectively controlled. Liquid crystalline properties provide a viable tool to govern the large and small scale order of the system by passing from one phase state to another on changing the temperature. Indeed, many groups have previously employed liquid crystalline organic semiconductors (LC OSCs) to explore the link between the molecular order and the performance of the material since the discovery of the photoconductivity in LC OSC[29].

Doping of LC OSCs was thoroughly explored in discotic LCs, for example n-type OSC perylene tetracarboxylic bisimide (PTCBI) derivatives[30] and ambipolar hexalkyloxytriphenylene derivatives (HAT family)[31]. It was demonstrated that chemically reduced thin films of a polymerizeable PTCBI derivative maintained conductivity anisotropy after doping[32], which is one of the characteristic properties of the LCs. HAT6 doped with a Lewis acid[33] demonstrated enhanced electric conductivity without mesophase degradation and enabled observation of charge transport anisotropy by AC conductivity measurements on aligned samples.

In this work we investigate the efficiency of molecular doping and compatibility of liquid crystalline matrix with an electron acceptor. First, we perform DSC, POM and X-ray scattering in order to investigate the impact of dopant introduction on mesophase stability. The spectroscopic measurements allow us to confirm the interaction between the host LC OSC and the electron acceptor. Further investigation of hole transport in mesophase underlines the correlation between induced structural changes and the impact of molecular geometry in regard to charge carrier mobility.

2 Materials and instrumentation

One of the most widely known LC OSC is the 2-dodecyloxy-6-(4-octylphenyl)-naphthalene (**8-PNP-O12**, Figure 1, a) exhibiting Smectic B (Sm_B, 66 °C to 101 °C) in which the molecules are organized in distinct layered structure and possess pronounced positional order in a hexagonal motive and Smectic A (Sm_A, 101 °C to 121 °C) mesophase which occurs on higher temperature and has similar layered organization, but the short-range hexagonal pattern is no longer relevant for this phase, the molecules are organized more randomly within the same smectic layer. This difference of intermolecular order is well-represented by the hole mobility: in the order of $1 \times 10^{-3}\,cm^2\,V^{-1}\,s^{-1}$ in the Sm_B mesophase and almost an order lower in the Sm_A mesophase ($3.5 \times 10^{-4}\,cm^2\,V^{-1}\,s^{-1}$). The **8-PNP-O12** can be regarded as the model substance for the rod-like LC OSCs[34–39]. This substance was employed as the host OSC in the current study and was used as supplied by SYNTHON Chemicals GmbH & Co. KG (Chemie Park Bitterfeld Wolfen, Germany), 99% purity.

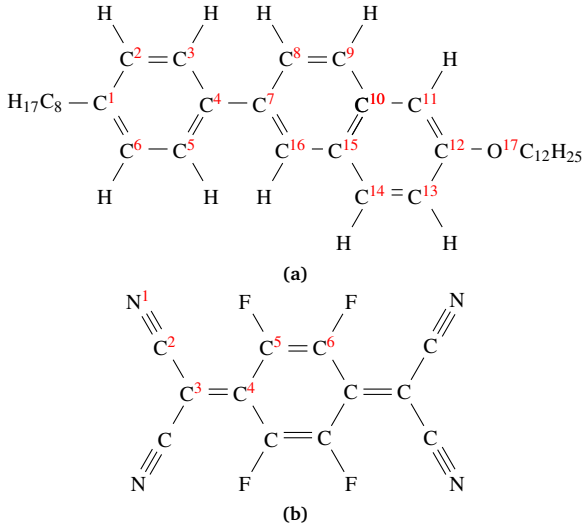

Fig. 1 Molecular structure of (a) 2-dodecyloxy-6-(4-octylphenyl)-naphthalene (**8-PNP-O12**) and (b) 2,3,5,6-tetrafluoro-7,7,8,8-tetracyanoquinodimethane (**F_4TCNQ**).

As the electron acceptor, we have used the fluorinated derivative of TCNQ (tetracyanoquinodimethane), the 2,3,5,6-tetrafluoro-7,7,8,8-tetracyanoquinodimethane (**F_4TCNQ**, Figure 1, b). The substance was provided by Apollo Scientific (Bredbury, United Kingdom), 97% purity. The molecules from tetracyanoquinodimethane family are well-known for their relevance for the field of OSCs and have been previously employed in discotic semiconducting liquid crystals[31] in an attempt to improve hole transport. Their effects on optoelectronic properties were also studied in nematic[40] and ferroelectric LCs[41].

Phase thermograms were obtained by a standard differential scanning calorimetry (DSC) experiment using a TA Instruments Q1000 Differential Scanning Calorimeter. Polarized optical mi-

croscopy (POM) was carried out with Olympus BX60F5, Linkam LTS 350 hotstage was used to control the temperature. Wide-angle x-ray scattering data was obtained with Forvis Technologies instrument. The x-ray source was 30 W Genix 3D (Cu anode, $\lambda = 1.5405$ Å and $E = 8.05092$ keV), the detector was Dectris Eiger R 1M. The beam size was $0.8 \times 0.8\text{mm}^2$, the x-ray flux was 4×10^7 photons/s and sample-to-detector distance was 190 mm. The d-spacing values (d) were calculated by using the relation $d = \frac{2\pi}{q}$, where q is the magnitude of the scattering wave-vector.

DFT calculations were performed with the help of *Gaussian 16*, Rev. A03 software[42]. Optical absorption spectra were recorded with Varian (Agilent) Cary 100 UV-Vis spectrophotometer in a standard 1 cm fused quartz cuvette. Raman spectra were recorded on Horiba LabRAM HR spectrometer with 4 mW and 785 nm excitation wavelength, the temperature was controlled with Linkam TMS 600 hotstage.

The electronic transport is characterized in liquid-crystalline phase with the time-of-flight (TOF) method[43]. The experimental setup consisted of a Nd:YAG laser ($\lambda = 355$ nm, pulse width = 5 ns), voltage source (Keithley 6487), current shunt resistor, voltage amplifier (Stanford Research SR560) and digital oscilloscope (Keysight DSO-X3022T).

3 Results and discussion

3.1 Phase behavior and texture

Five mixtures were prepared by mixing selected weight fraction of dopant of 0.1 (**c1**), 0.5 (**c2**), 1 (**c3**), 3 (**c4**), 5 (**c5**) %wt. with host material in chloroform solvent in glass vial at 50 °C for 1 hour. Vials then were left open for 24 hours under vent hood to ensure complete solvent evaporation.

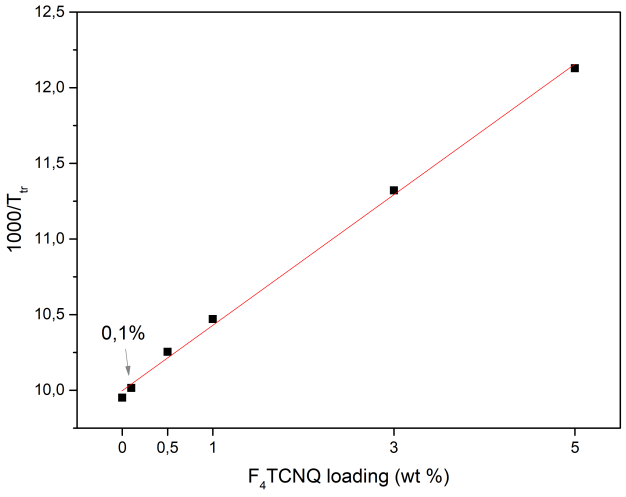

Fig. 2 Plot of inverse transition temperature (1000/T_{tr}) from the Sm_A to Sm_B phase as a function of **F$_4$TCNQ** concentration.

As a first step, we have performed DSC over the whole sample sequence in order to ensure mesophase stability over its temperature range. Figure 2 allows us to observe the transition temperature between Sm_A and Sm_B of composite samples and compare it to pure **8-PNP-O12**. This transition is affected the most by the presence of **F$_4$TCNQ** and its temperature is inversely proportional to its concentration. Interestingly, the composites exhibit relatively minor changes in crystallization and complete melting temperatures(Figure 1 of Supplementary Materials).

POM allowed us to observe the texture of composites (Figure 3). The presence of **F$_4$TCNQ** appears to have little effect on the texture of the both Sm_B and Sm_A mesophases: the characteristic focal conic pattern is preserved in all composites (textures of all samples are assembled in Figures 2.1 and 2.2 of Supplementary Materials) and the size of liquid crystalline domains decreases as the **F$_4$TCNQ** content is increased. Observed behavior allows us to propose good overall compatibility between the **8-PNP-O12** and **F$_4$TCNQ**.

One can notice the color change, which becomes more apparent on higher concentrations (Figure 3, c and d): the color of the cells filled with composites itself exhibits notable shift towards blue, though neither of initial products has this color. This coloration can be regarded as a result of interaction between **8-PNP-O12** and **F$_4$TCNQ**. To better explore this, we have performed UV-Vis-NIR optical spectroscopy, which we are going to cover further.

3.2 X-ray scattering

1D data extracted from wide-angle x-ray scattering images (inset of Figure 4) shows the characteristic peaks corresponding to the Sm_B and Sm_A mesophases: one peak (b) corresponding to the pseudo-hexagonal order inside of the smectic layer about $1.39\ \text{Å}^{-1}$ ($d = 4.56$Å) and another peak (a) corresponding to the layered structure of smectic phase around $0.17\ \text{Å}^{-1}$ ($d = 36.96$Å). The latter appears in both the Sm_B and Sm_A mesophases. The calculated length of the **8-PNP-O12** molecule (35.58 Å) allows us to suggest mono-layer structure for these mesophases.

The Sm_B positional order distance (peak b) feebly increases with temperature, however it is found to be indifferent to the content of the **F$_4$TCNQ**(Figure 3.2 of Supplementary Materials). We have calculated the full width at half maximum (FWHM) values, which correspond to the distribution of the intermolecular distance inside of the Sm_B layer. Figure 4 demonstrates the dependence of FWHM of peak **b** as a function of dopant concentration at 85 °C (Sm_B). It is found that this value increases with the concentration of **F$_4$TCNQ**, which signifies an increase of the number of deviations from the characteristic intermolecular distance in the bulk of the sample. One can conclude that the presence of **F$_4$TCNQ** acts as an impurity leading to a decrease of the order in the plane of the Sm_B layer.

The small-angle part of the data demonstrates a more complex picture of the 2D-layered structure of the smectic mesophase (inset of Figure 5). Multiple peaks appearing in the 1D data could be attributed to the "ripple" in plane of the smectic layer which results in a so-called modulated smectic mesophase. Such structures are encountered in lyotropic[44] as well as thermotropic[45,46] LCs and are not uncommon for assymetric molecules exhibiting longitudinal torsion[47]. The leftmost intense peaks (a_4 and a_4^*, inset of Figure 5) are attributed to the direction orthogonal to the layer plane and can be utilized to extract the smectic interlayer distance, when the satellite peaks (a_1-a_3 and a_1^*-a_3^*, inset

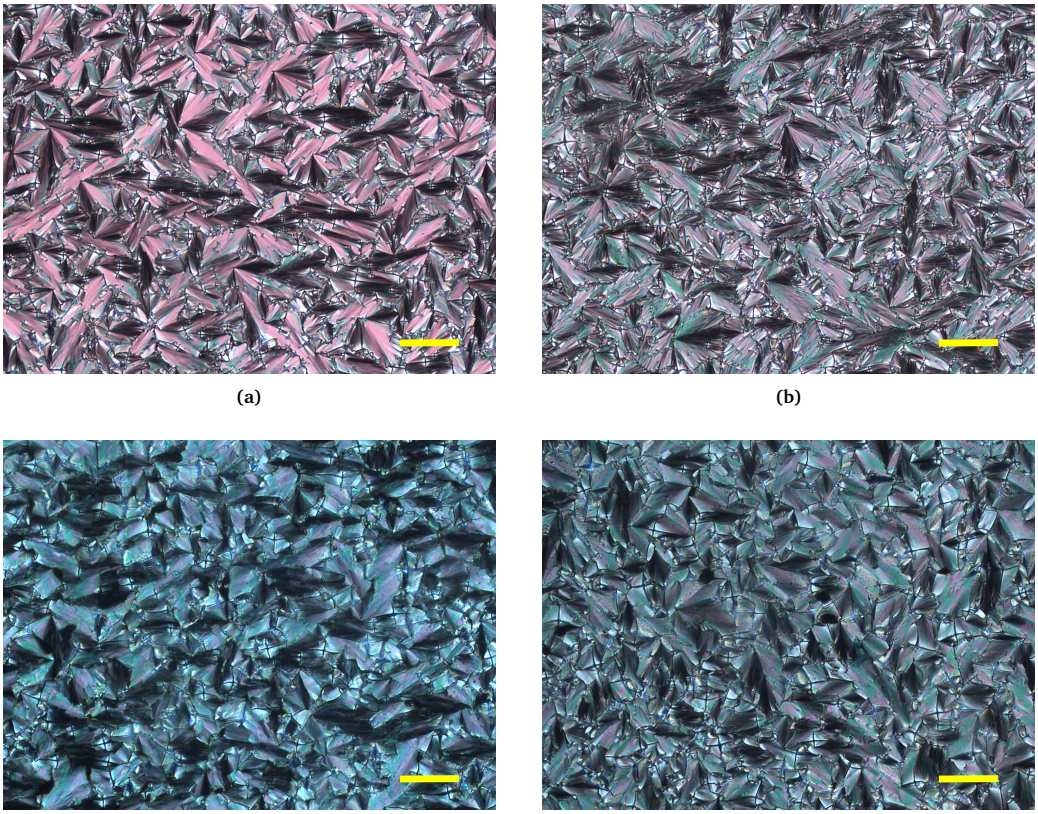

Fig. 3 Sample texture under crossed analyzer-polarizer: for pure **8-PNP-O12** (in Sm_B at 85 °C (a) and Sm_A mesophase at 115 °C (b))and **c5** (in Sm_B (c) and Sm_A (d) mesophase). Scale bar represents 100 μm.

of Figure 5) correspond to the layer modulation. Figure 5 allows us to compare the smectic layer separation distance for pure **8-PNP-O12** and prepared composites. The value is found to be slightly greater than the length of **8-PNP-O12** molecule in Sm_B, and slightly smaller in Sm_A, indicating some interpenetration of layers. The layer spacing is found to be proportional to the content of **F_4TCNQ**: as previously deduced from the intermolecular distance distribution (Figure 4), the layers become less condensed

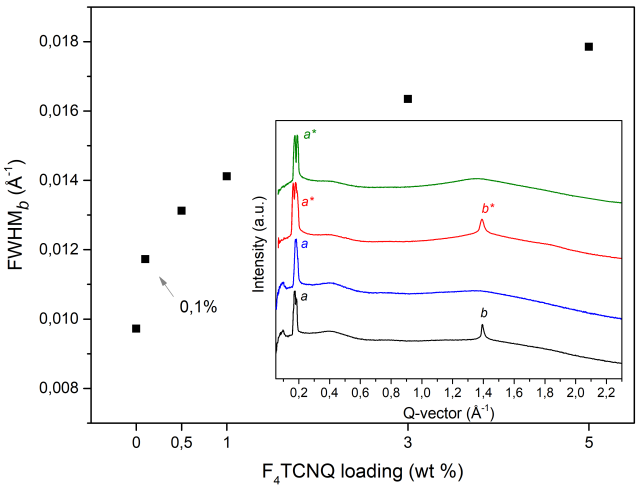

Fig. 4 Plot for FWHM of Sm_B in-layer order peak as a function of **F_4TCNQ** content. Inset: 1D WAXS data at 85 °C (Sm_B) for pure **8-PNP-O12** in Sm_B at 85 °C (black line), in Sm_A mesophase at 115 °C (blue line) and **c5** in Sm_B at 85 °C (red line), in Sm_A mesophase at 115 °C (green line) .

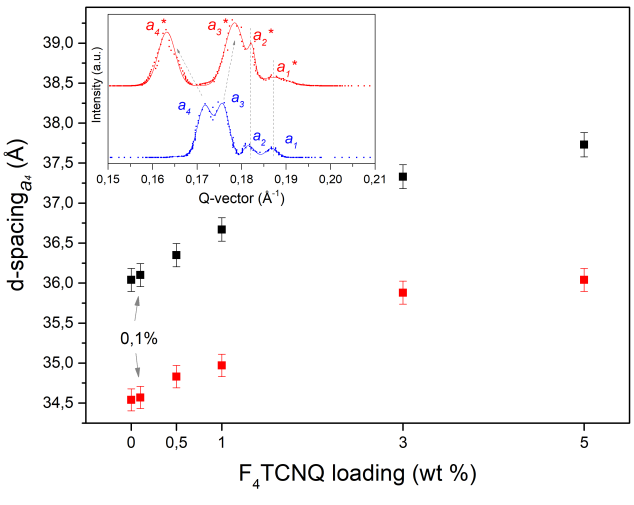

Fig. 5 Plot for smectic layer spacing as a function of **F_4TCNQ** content in Sm_B at 85 °C (black squares) and in Sm_A mesophase at 115 °C (red circles). Inset: small-angle part of 1D WAXS data at 85 °C (Sm_B) for pure **8-PNP-O12** (in blue, layer spacing $d = 36.12$ Å) and **c5** (in red, layer spacing $d = 37.73$ Å).

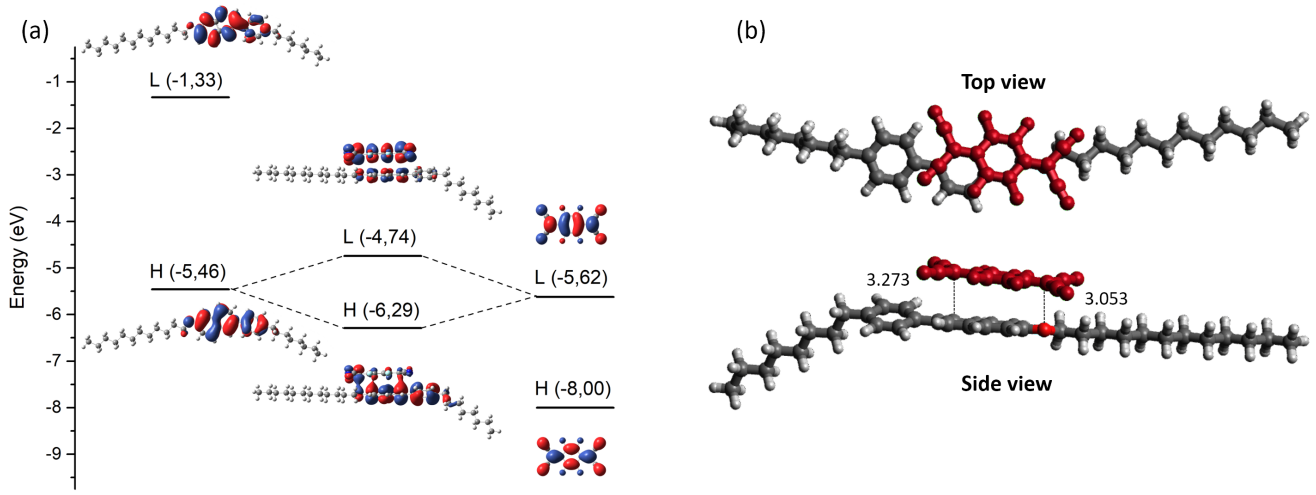

Fig. 6 (a) Energy diagram of frontier molecular orbital levels for **CTC** and isolated molecules of **8-PNP-O12** and **F_4TCNQ**. MO levels of pristine substances are calculated on B3LYP/6-31++G(d,p) level; (b) **CTC** of **8-PNP-O12** and **F_4TCNQ**, geometry optimized and MO levels calculated on B3LYP-D/6-31++G(d,p) level. Interatomic distances are shown in Å.

as the doping ratio increases, which promotes greater layer flexibility and subsequently decreases the overall order of the composites[48] (Figure 3.3 of Supplementary Materials).

3.3 Spectroscopic study of charge transfer complex

Doping of some OSCs results in the apparition of ionized states within the bulk of the OSC. However, it has been recently demonstrated that this concept does not apply to every OSC. When an intermolecular charge transfer takes place, two possible options are usually considered[6]: so-called integral charge transfer (ICT) and partial charge transfer (PCT). The concept of ICT has dominated the field: classic OSCs with relatively shallow band gap and high lying HOMO, like poly(3-hexylthiophene) (P3HT), is a good example[49]. However, not every OSC with an appropriate level of HOMO will forcibly undergo an integral charge transfer: Mendez et al.[50] has confronted the ICT in P3HT - **F_4TCNQ** system with the observable PCT signs for the quaterthiophene (4T) oligomer. The charge transfer degree for 4T was only of 0.24[50] as compared with that of fully ionized P3HT.

The concept of partial charge transfer applies a more elaborated approach. Two molecules (donor and acceptor) form a so-called charge transfer complex (**CTC**) which regarded from the supramolecular point of view: the electron pair from the donor's HOMO is not entirely transferred to the LUMO of the acceptor, but is situated on a new supramolecular orbital which is formed during the complex "bonding"[16]. This MO has lower energy than initial HOMO of the donor and LUMO of the acceptor, which makes the complex state more beneficial and thermodynamically stable. Thus, the electron neither truly leaves the HOMO of the donor nor is fully transferred to the LUMO of acceptor, but is continuously "shared" between two[7]. This approach may also explain the remarkable thermodynamical stability of the **CTC** encountered in the present work.

Both cases (ICT and PCT) result in noticeable change of electronic configuration of the host OSC moiety. It is possible to observe such changes by conventional spectroscopic methods. Furthermore, by the means of *ab initio* calculations it is possible to predict the character of this charge transfer[27]. In our study, the experimental results obtained from spectroscopy are confronted to those of DFT calculations. This comparison provides us the basis to validate the predicted geometry for the **CTC** and utilize it to explain its effect on the charge transporting properties.

3.3.1 Computational study

Geometries of pristine **8-PNP-O12**, **F_4TCNQ** and the CTC were firstly optimized by semiempirical methods with further DFT optimisation on B3LYP/6-31++G(d,p) level with additional empirical dispersion corrections (GD2) for the **CTC**. This have proven itself to significantly enhance[51] the accuracy of systems which involve intermolecular charge transfer. Optimized geometry had zero imaginary frequencies.

The molecular orbital diagram for **CTC** and its initial products (Figure 6, a) shows successful hybridisation of the HOMO of the **8-PNP-O12** and the LUMO of the **F_4TCNQ** into a novel *intra*molecular bonding orbital at -6.29 eV. As a result of complex "bonding", the geometry of its components undergoes some noticeable change. **F_4TCNQ** molecule now exhibits some deviation of planarity (minor longitudinal torsion). For the **8-PNP-O12**, a quite significant point is the change of the dihedral angle 5-4-7-8 (Figure 1, a), which changes from 141.57 to 155.83°.

The top view on the optimized geometry (Figure 6, b) demonstrates good alignment of the quinoid ring of the **F_4TCNQ** with one of the naphthalene rings of **8-PNP-O12**. The bond lengths of quinoid ring and naphthalene in the **CTC** undergo some expected change: quinoid system approaches aromaticity upon allocation of the transferred "part" of the electron, the opposite is true for the aromatic system of the naphthalene (Figures 4.1 and 4.2 of the Supplementary materials). The geometry of neutral **8-PNP-O12** is not planar, since it has some noticeable torsion angle between phenyl and naphthalene parts. Due to this fact, the

F_4TCNQ molecule is not able to align itself completely parallel to the aromatic system of **8-PNP-O12**, which results in the intermolecular distance between **8-PNP-O12** and **F_4TCNQ** to be found in a range between 3.273 and 3.053 Å (Figure 6, b, side view). This fact presumably contributes to the significant asymmetry of the shape of the HOMO of **CTC** as compared to that of more planar donor substances [50].

The **CTC** is calculated to have a bandgap of about 1.55 eV. Thus, it is then expected for the **CTC** to exhibit optical absorption in near infrared (NIR) part of the spectrum. UV-Visible-NIR spectroscopy is a suitable tool to investigate the character of newly formed **CTC**, given the absence of any electron transitions for initial products [50,52] in the NIR range.

3.3.2 Optical spectroscopy

Since the **CTC** forms new supramolecular orbitals with their own energy levels and bandgap, there should exist dedicated electron transition energy levels. In theory, it should be possible to observe the signature of **CTC** in the UV/Vis spectrum. Previous works, conducted on P3HT [6,50] have shown that it is indeed possible to observe the sharp peaks of fully ionized **F_4TCNQ**$^-$ in case of ICT. P-doping of discotic LC HAT6 with **F_4TCNQ** has also demonstrated distinctive absorption features in both crystalline phase and columnar mesophase [31].

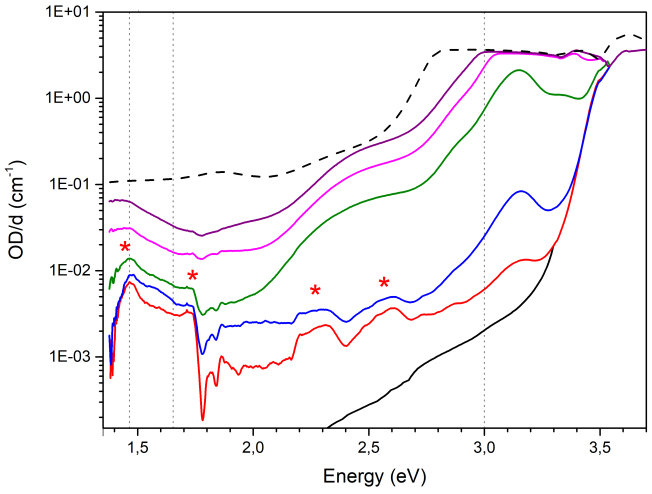

Fig. 7 UV-Vis spectra for prepared composites and starting products taken in 2 mg ml^{-1} chloroform solution: pure **8-PNP-O12** (solid black line) and **F_4TCNQ** (dashed black line), **c1** (red), **c2** (blue), **c3** (green), **c4** (pink) and **c5** (purple) composites. Gray vertical dotted lines correspond to the expected energies of the anion **F_4TCNQ**$^-$ absorption peaks [50,53]. Peaks assigned to **CTC** are marked with red asterisks.

Pure **8-PNP-O12** exhibits optical absorption in UV region, which is explained by its wide optical bandgap [37]. **F_4TCNQ** in turn, has it absorption onset at 2.6 eV, which leaves the remaining part of optical spectrum isolated and allows comfortable observation of their interaction product (**CTC**). The absorption spectra of initial products as well as the composites are assembled in Figure 7.

We are able to observe neutral **F_4TCNQ** signatures on higher concentrations, however it is possible to notice some new absorption peaks situated in the near infrared part of the spectra which are not present for the initial materials. The optical density of these new peaks seems to be in good agreement with the content of **F_4TCNQ**.

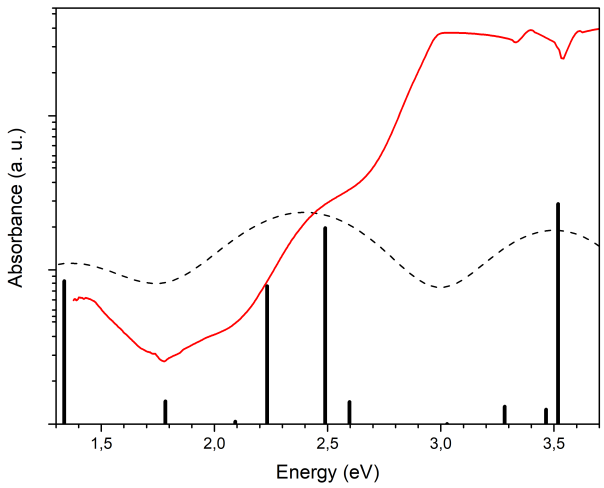

Fig. 8 UV-Vis spectrum of **c5** composite (solid red line) and the result of TD-DFT calculation of **CTC** (dashed black line). Black vertical lines denote transition energies and corresponding oscillator strengths.

The anion of **F_4TCNQ** has optical absorption bands at 1.45 eV, 1.65 eV and 3 eV [53,54]. Sharp features observed on these energy levels would propose the ICT mechanism. It is possible to observe one peak at 1.45 eV, however the other peaks at 1.65 eV and around 3 eV (expected in case of ICT) are absent, instead, we observe a shoulder at 1.72 eV, as well as some new features in the visible part (two distinct absorption bands at 2.27 eV and 2.57 eV are observed on low concentrations and further convolute in a shoulder at larger dopant load). As illustrated by Mendez et al. [50], for PCT case the absorption peaks of **CTC** may be situated on different photon energy values.

We have performed TD-DFT calculations in order to gain insight on the observed results. Observations of calculated optical absorption spectra (Figure 8) allows us to assign previously observed peaks in near infrared (peak at 1.45 eV with a sharp shoulder around 1.75 eV) and visible (two peaks at 2.27 eV and 2.57 eV) parts of spectrum (Figure 7) to the presence of **CTC** in the solution.

These observations allow us to confirm the partial charge transfer between the **8-PNP-O12** and **F_4TCNQ**. However, the optical signatures of pristine **F_4TCNQ** are still present in the mixture.It is possible to suggest that solvation effects may somewhat hinder the process of charge transfer, or the resulting **CTC** has lower solubility in chloroform than initial products.

3.3.3 Vibrational spectroscopy

We have carried out Raman spectroscopy in all the 4 phase states of composites:

$$\mathbf{Cr} \rightarrow \mathbf{Iso} \rightarrow \mathbf{SmA} \rightarrow \mathbf{SmB} \rightarrow \mathbf{Cr}^*,$$

The first spectrum was recorded in crystalline phase **Cr**, then the sample was heated to isotropic phase **Iso**, where it was maintained for 30 minutes. After annealing, each sample was slowly cooled back to crystalline phase (hereafter Crystalline annealed, **Cr***) through Smectic A (**SmA**) and Smectic B (**SmB**) mesophases, respectively. Raman spectra were recorded in every phase state, as well as two times in crystalline phase (before and after annealing). This was done in order to confirm the charge transfer and to investigate the thermal stability and possible influence of mesophase on the **CTC**.

In previous section, we have noticed that **CTC** has optical absorption in near-infrared part of the spectrum (Figure 7). The energy of excitation irradiation (1.58 eV) seems to be in resonance with one of the electron transition energies of **CTC**, which can explain little to no signature of initial products in the spectra recorded during annealing, as well as for the annealed composite (Figure 9 for **c5**), despite the huge excess of pristine **8-PNP-O12** which is expected to contribute to the Raman spectrum.

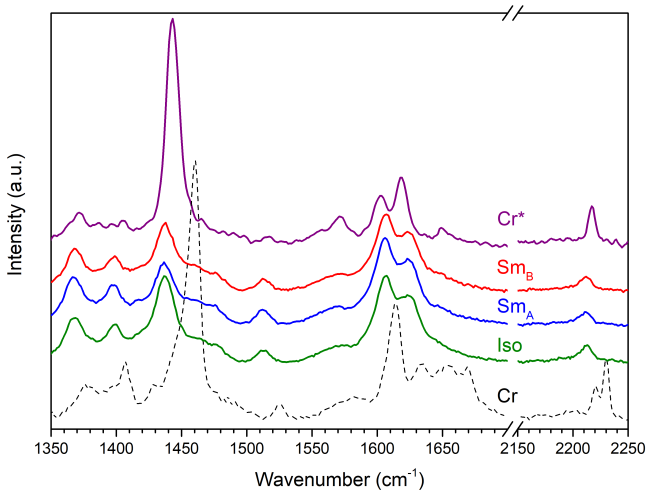

Fig. 9 Raman plots for **c5** composite in different phase: black dashed for as-prepared powder, green for I, blue for Sm_A, red for Sm_B and purple for annealed Cr. Intensity is normalized for naphthalene ring stretch band ($1635\,cm^{-1}$ before annealing, $1624\,cm^{-1}$ in liquid and liquid crystalline phase and $1618\,cm^{-1}$ after annealing).

Firstly, we describe the case of the freshly prepared composite (Figure 9, **Cr**). The spectrum exhibit strong signatures of pristine **F$_4$TCNQ**, notably the isolated vibrational bands of nitrile group (symmetric and assymetric stretching of 1-2 bond, Figure 1, b) at 2220 and 2228 cm^{-1}, as well as quinoid part (lateral double bond 3-4 and ring 5-6, Figure 1, b at 1458 and 1668 cm^{-1}, respectively). The only new feature noticeable in this spectrum is a new band at 1654 cm^{-1} between the aforementioned quinoid ring stretch band and naphthalene ring (7-16 at Figure 1, a) stretching at 1634 cm^{-1}.

The situation changes significantly upon transitioning to isotropic phase (Figure 9, **Iso**). The nitrile group peak is shifted to the left 2212 cm^{-1} and broadened. The quinoid ring stretching band disappears, and stretching of lateral double bond shifts to the left (1437 cm^{-1}). Peaks, related to the aromatic system (phenyl and naphthalene rings stretching) of **8-PNP-O12** also undergo noticeable shift to the left (1606 and 1624 cm^{-1}, respectively). Interestingly, the spectra recorded in SmA and SmB phases (Figure 9, **SmA** and **SmB**) seem to bear no difference with each other.

Finally, after crystallizing from Sm_B mesophase, the annealed crystalline sample shows (Figure 9, **Cr**$*$) correlation to the spectra, previously observed during annealing as we can notice in more pronounced peaks of aromatic system of **8-PNP-O12** (1600 and 1619 cm^{-1}), as well as the reappeared shifted band connected to the quinoid ring (1650 cm^{-1}). Other samples exhibit similar behavior (comparison of spectra before and after annealing is assembled in Figure 5, Supplementary Materials). Smaller concentrations exhibit less pronounced effects due to strong contribution of initial products. General trend, observed in these plots allows us to suggest successful formation of charge transfer complex between the host and the dopant.

These experimental spectra suggest that the **CTC** is thermodynamically stable in applied temperature range of 50 °C to 130 °C and all phase states exhibited by the composites, which is in good agreement with the observations of Khan et al[31], where optical absorption spectrum recorded in isotropic phase (120 °C) looked similarly to other phase states. Moreover, there seem to be no observable influence of mesophase structure on the quantity of the charge transfer between **8-PNP-O12** and **F$_4$TCNQ**: vibrational bands positions do not change between Sm_B and Sm_A mesophases. It is of interest to compare this observation to the case of PTCBI derivative[55,56], where a phase transition introduces a striking change in spectroscopic properties of the material, attributed to the shift in π-π overlap between the neighboring molecules due to the intermolecular longitudinal offset, which is induced on the phase transition. In our case, the transition from Sm_B to Sm_A mostly affects the positional order and does not induce any significant layer deformation, thus the **CTC** remains undisturbed. Weak signatures of **CTC** in pre-annealed samples allow us to emphasize the role of annealing in preparing of such type of composites. Simple mixture of initial substances in a solvent seems to be not quite efficient, and melting of host **8-PNP-O12** is able to provide more intimate contact between two components of **CTC**, which is necessary for "bonding".

The role of vibrational spectroscopy in the study of charge transfer related to **F$_4$TCNQ** and its homologues is undeniable[50–53,57,58]. The vibrational analysis of the charge transfer is based on the shift of nitrile band, since this vibrational band is situated in the part of the spectrum which is usually isolated: it does not contain any other vibrational modes of initial products.

It seems that a vast number of research groups favor IR spectroscopy over Raman[15,59,60]. In fact, pristine **F$_4$TCNQ** molecule exhibits 4 vibrational modes in this region of the spectrum (2100 cm^{-1} to 2300 cm^{-1}), with two of them being IR active (b_{2u} and b_{1u} at 2213 cm^{-1} and 2227 cm^{-1} [51], respectively), and the other two - Raman active (b_{3g} and a_g at 2219 cm^{-1} and 2227 cm^{-1} [57], respectively). We demonstrate that Raman spectroscopy is able to provide us useful information in case PCT[51] and also allows us to choose an excitation wavelength for potential resonant effects.

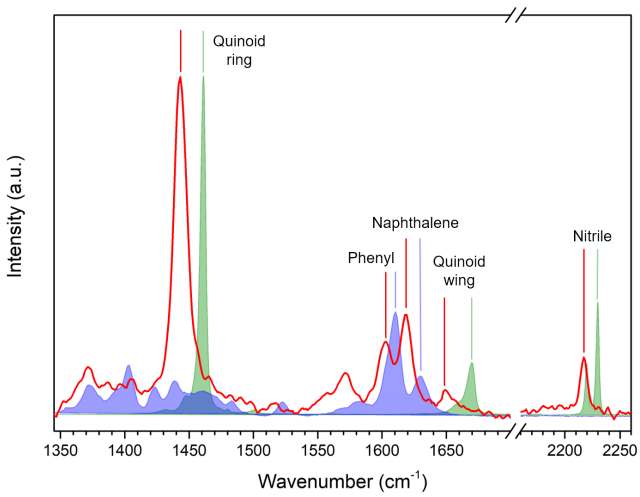

Fig. 10 Raman plots for **Cr*** of **c5** composite (red solid line), pure **8-PNP-O12** (blue filled plot) and pure **F_4TCNQ** (green filled plot) recorded at room temperature. The Raman bands of interest are labeled with the corresponding color.

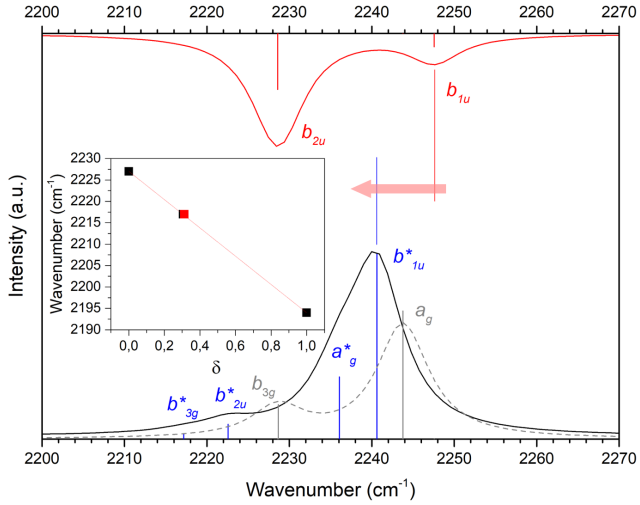

Fig. 11 Calculated vibrational spectra (scaling factor of 0.9626[61,62]) for pure **F_4TCNQ** (Raman in dashed gray and IR in solid red) and **CTC** (Raman in solid black and vibrational frequencies in blue). The corresponding vibrations are assigned respectively. **Inset:** Graphical representation of b_{1u} vibrational frequency as a function of charge transfer degree. Black points corresponding to **F_4TCNQ** and **F_4TCNQ$^-$** indicate frequencies extracted from IR spectroscopy[49,50]. Frequency corresponding to partial charge transfer is extracted from Raman spectrum. The point in red represents the expected amount of charge transfer from the DFT calculations.

Further, we present the spectra of **c5** composite, since it provides the best signal-to-noise ratio of the modes related to the **CTC** presence. Figure 10 represents the comparison between the Raman spectra of annealed **Cr*** of **c5** composite with initial products (pure **8-PNP-O12** and **F_4TCNQ**). Some noticeable red shift occurs to the bands assigned to the aromatic system of **8-PNP-O12** and quinoid as well as nitrile parts of the **F_4TCNQ** molecule. However, it is difficult to estimate the individual contribution of lower frequency vibrational bands, since they are located in tighter groups, and their intensity is relatively low.

In fact, due to previously discussed change in molecular geometry the mutual exclusion rule which is valid for **F_4TCNQ** and **F_4TCNQ$^-$** (they belong to D_2h symmetry group[53]) does no longer apply to the vibrational modes exhibited by **CTC**, which was predicted by Zhu and coworkers[51]. DFT frequency calculations show significant polarizability change (in fact, of higher magnitude than inherent Raman modes b_{3g} and a_g) which occurs on vibrational mode previously attributed as b_{1u} for symmetrical molecules (for convenience labeled b^*_{1u}). The resulting Raman intensity at 785 nm excitation of the b^*_{1u} band (around 2241 cm^{-1} in Figure 11, linear scaling factor of 0.9626[61,62] is applied) is even greater than of normally expected a^*_g. This fact allows us to assign the peak observed at 2217 cm^{-1} (Figure 10) to the now Raman-active vibrational mode b^*_{1u}.

This conclusion also allows us to directly compare the observed vibrational mode b^*_{1u} to frequencies of those b_{1u} modes which are only IR-active in **F_4TCNQ** and **F_4TCNQ$^-$** (since it no longer posses a center of symmetry). We perform a quantitative estimation of the charge transfer degree δ between **8-PNP-O12** and **F_4TCNQ** using the following equation[63]:

$$\delta = \frac{2\Delta\nu}{\nu_0}\left[1-\frac{\nu_1^2}{\nu_0^2}\right]^{-1}, \qquad (1)$$

where the observed shift in vibrational frequency ($\Delta\nu$) is compared to the position of the same band in pure **F_4TCNQ** (ν_0) and the anion **F_4TCNQ$^-$** (ν_1).

The value for frequency of b_{1u} mode for **F_4TCNQ$^-$** is taken to 2194 cm^{-1} [49,50]. The observable red shift of this band (2227→2217cm^{-1}) yields a charge transfer degree of **0.31**, which is in excellent agreement with DFT calculations (value of 0.31 obtained as an average of electrostatic potential (**ESP**, 0.33), natural bond orbital (**NBO**, 0.32) and Hirshfeld population (**CM5**, 0.29) analysis schemes). Inset of the Figure 11 allows us to compare the calculated value (red) with the one extracted from the Raman spectrum (black).

3.4 Charge carrier transport

It is usually assumed that introduction of dopant results in increase of notoriously weak intrinsic "free" charge carrier density in organic substances, though its effects on bulk mobility need to be addressed more profusely. In this section we have made an attempt to disclose the influence of charge transfer complex on bulk hole mobility of **8-PNP-O12**.

The TOF technique has been previously applied to a vast number of LC OSCs[64–68] and has proven itself as a reliable tool of charge carrier mobility determination. Due to the nature of this technique, the obtained results are decoupled from the absolute number of charge carriers which participate in the transport (quantity of carriers impacts the magnitude of signal, not the photocurrent decay profile). Mobility (μ) is calculated by using the equation[43]:

$$\mu = \frac{d}{\tau_{tr}E}, \qquad (2)$$

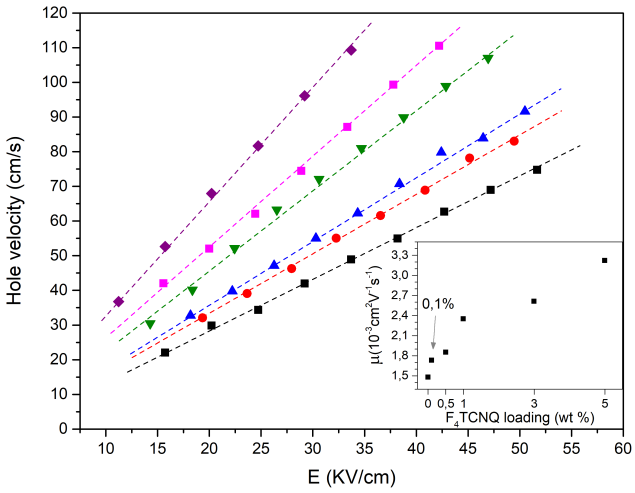

(a)

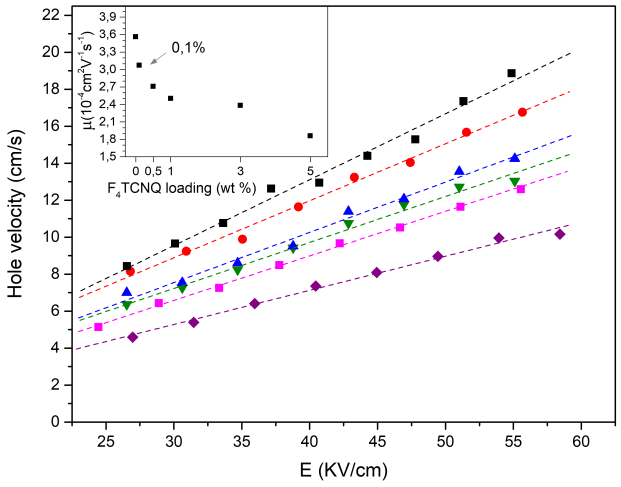

(b)

Fig. 12 Plot of the hole velocity as a function of applied electric field for pure **8-PNP-O12** (black squares), **c1** (red circles), **c2** (blue triangles), **c3** (green triangles), **c4** (magenta squares) and **c5** (purple diamonds) in Sm_B mesophase at 85 °C (a) and Sm_A mesophase at 115 °C (b). **Insets:** Plot of hole mobility as a function of **F_4TCNQ** content at corresponding temperature.

Where d is the distance between electrodes, τ_{tr} is the charge carrier transit time, E is the applied electric field.

Hole mobility values are calculated for the range of applied electric field E from $10\,\mathrm{kV\,cm^{-1}}$ to $50\,\mathrm{kV\,cm^{-1}}$ in Sm_B mesophase and $25\,\mathrm{kV\,cm^{-1}}$ to $60\,\mathrm{kV\,cm^{-1}}$ in Sm_A mesophase, the sample thickness was about $9\,\mu$m (sample cells were individually calibrated prior to filling by means of an impedance analyzer).

Figure 12 assembles the plots of hole velocity (direct comparison of transient photocurrent plots can be found in Figures 6.1 and 6.2 of Supplementary Materials) as a function of applied electric field in two different mesophases of the sample. It should be noted that all composites retain the linearity of carrier velocity distribution, observed for the pure **8-PNP-O12**, as well as other similar compounds.

Interestingly, the composites exhibit different trends in each mesophase: in Sm_B, the hole velocity is directly proportional to the content of introduced **F_4TCNQ**; however in Sm_A the situation is opposite. Since we have previously illustrated the thermodinamical stability of the CTC (Figure 9: the Raman spectra recorded in isotropic, Sm_A and Sm_B are identical in terms of band positions and relative intensity), it is possible to suggest that observed behavior is a result of some changes in the mesophase structure, not in the interaction between the **8-PNP-O12** and **F_4TCNQ**. It seems that **CTC** is able to promote hole transport in Sm_B mesophase (Inset of Figure 12, a) and impede it in Sm_A (Inset of Figure 12, b). It is also noteworthy to mention that with increasing of dopant content the signal-to-noise ratio of TOF transient current is deteriorating (Figures 5.1 and 5.2 of the Supplementary materials). This can be explained due to the expected shift of the MO level energy of the sample by the present **CTC** moieties closer to the work function of the electrode material (ITO)[8], which results in easier charge injection and subsequent rise of the DC conductivity (Figures 7.1 and 7.2 of the Supplementary Materials).

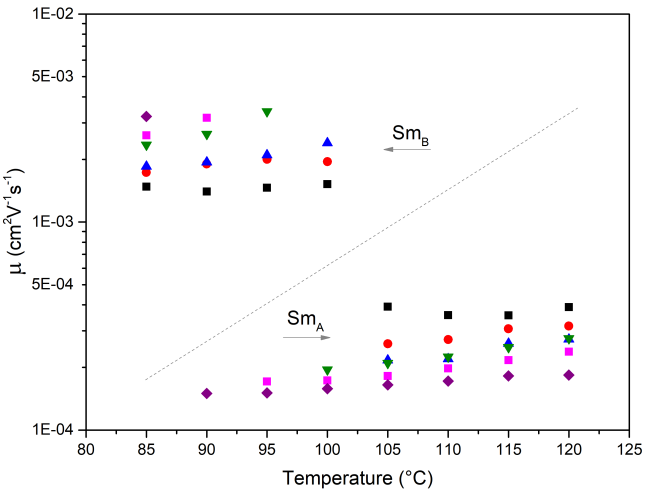

Fig. 13 Plot of the hole mobility as a function of temperature for pure **8-PNP-O12** (black squares), **c1** (red circles), **c2** (blue triangles), **c3** (green triangles), **c4** (magenta squares) and **c5** (purple diamonds).

Hole mobility as a function of temperature is presented in the Figure 13. Results obtained for pure **8-PNP-O12** are in good agreement with previously reported[38,69]: hole mobility of $1.5\times10^{-3}\,\mathrm{cm^2\,V^{-1}\,s^{-1}}$ in Sm_B and $3.6\times10^{-4}\,\mathrm{cm^2\,V^{-1}\,s^{-1}}$ in Sm_A, temperature-independent for a given mesophase. As we have previously noticed, doping with **F_4TCNQ** results in increase of hole mobility in Sm_B, and decrease in Sm_A, however this time the mobility seems to be increasing with the temperature. This can be explained by the fact that CTC is interfering with the mesophase, thus creating some trap states[70]. These trap states can be overcome on higher temperature due to broadening of the density of states (DOS) distribution[28,71]. We have calculated the activation energy for mobility E_a in both mesophases (Figure 14). It is found that in Sm_B the E_a is increasing with dopant concentration, when in Sm_A it is decreasing.

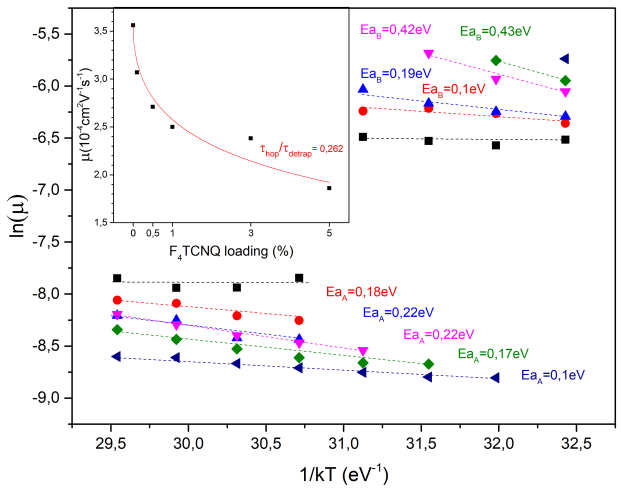

Fig. 14 Plot of the activation energy of the hole mobility for pure **8-PNP-O12** (black squares), **c1** (red circles), **c2** (blue triangles), **c3** (green triangles), **c4** (magenta squares) and **c5** (purple diamonds). **Inset:** Fit of hole mobility in the Sm_A mesophase as a function of **F$_4$TCNQ** concentration with the equation 3 at 115 °C.

The behavior of the hole mobility in the Sm_A mesophase can be compared to the similar case of system consisted of **8-PNP-O12** doped with a dihexyl terthiophene (DH3T)[72], for which the hole transport was considerably affected by carrier trapping in both mesophases. Funahashi et al have introduced an equation which describes mobility behavior in their system:

$$\mu = \frac{\mu_0}{(1+\frac{\tau_{detrap}}{\tau_{hop}}C^{\frac{1}{2}})} \quad (3)$$

where μ_0 is the mobility in pristine **8-PNP-O12**, C is the dopant molar fraction, τ_{hop} and τ_{detrap} is the hopping time and detrapping time (when the carrier is released) respectively. For the **8-PNP-O12** doped with DH3T the ratio of τ_{hop} to τ_{detrap} was found to be around 8.6×10^{-4}, when in our case after fitting (inset of Figure 14) it is found to be substantially larger, about 0.26. It is then clear, that according to the assumptions of Funahashi et al, for holes trapped by D3HT it is significantly harder to leave their trapped state than for the case of doping by **F$_4$TCNQ**. This may be explained by taking into account the HOMO of D3HT which lies higher than that of 8-PNP-O12 (5.1 eV vs 5.6 eV); thus the D3HT indeed acts as a trap for the host **8-PNP-O12**. Results reported in this work demonstrate negative impact of this impurity on charge transport, up to complete loss of electronic transport in Smectic A mesophase on high dopant loading (and dominating ionic contribution). In our case, the HOMO of **CTC** lies lower (6.3 eV estimate from DFT calculations), thus acting as a potential barrier, not a trap. It is well-known for the potential barriers to have less negative effects on the carrier transport, since they repel carriers (when traps attract them), thus the carriers have more chances to find their way around the barrier instead of being held by a trap state[73].

The behavior of mobility in Sm_B is unexpected. Arkhipov et al.[74] have developed a model which is meant to explain the influence of doping impurity on the charge carrier mobility behavior in bulk OSCs. This model has been successfully applied to the doping of amorphous OSCs, for example P3HT, and may be applied to other materials which exhibit charge transport by carrier hopping (which is the case for **8-PNP-O12**). It describes two doping regimes in regard to the concentration of the dopant content in the OSC: it is proposed that the dopant is able to induce potential traps on low concentrations, where the dopant sites are essentially isolated. For increased concentrations, the overlap of these dopant-induced trap states is able to smooth the potential landscape of the material, and alongside with trap filling by increased charge carrier density, this may be held accountable for the mobility increase.

It is worth noting that due to the homogeneous alignment (i.e. the long molecular axis is parallel to the electrode plane) of the studied samples, the charge transport takes place within the smectic layers. Though the WAXS data demonstrates that the introduction of **F$_4$TCNQ** does not result in the increase of the structural order, the basic principles of the pristine **8-PNP-O12** mesophases are maintained in the prepared composites. Taking into account the pseudo-hexagonal close range order of the Sm_B mesophase[75], it is possible to propose that the **CTC** moieties are distributed more uniformly across the smectic layered structure (Figure 8 of the Supplementary Materials), contrary to the case of the Sm_A mesophase, where is no preferred order inside of the smectic layer. Thus, the short range order of the Sm_B mesophase is able to maintain the favorable overlapping of the potentials of adjacent **CTC** sites, resulting in improved charge carrier mobility inside of the smectic layer. However, in the less ordered Sm_A mesophase, **CTC** is allowed to be freely distributed or even aggregated inside of the layer, which results in the absence of overlapping between the potentials of neighboring **CTC** sites, and, as a result, charge carrier trapping.

Chen et al[73] have demonstrated that carrier density in doped PTCBI derivative is thermally activated. This may explain the mobility increase by trap filling in Sm_B and the rise of E_a, but the decrease of E_a in Sm_A with increasing **F$_4$TCNQ** content suggest that traps are generated faster than new carriers. This contradicts to some extent with the phase behavior of composites: the Sm_A to *Iso* transition temperature does not show significant shift with dopant concentration increase, which allows us to propose that the stability of Sm_A mesophase is less affected by the dopant presence than that of Sm_B.

4 Conclusion

In this work we have explored different aspects of a LC OSC - electron acceptor complex. We have confirmed the stability of LC mesophase up to significant concentrations of introduced **F$_4$TCNQ**. DFT calculations have allowed us to expect the partial charge transfer between the host **8-PNP-O12** and the acceptor **F$_4$TCNQ**, as well as some noticeable geometry change. Furthermore, we have predicted the behavior of **CTC** in optical and vibrational spectroscopy. We have confirmed that it is indeed possible to distinguish partial and integral charge transfer by UV-Vis-NIR spectroscopy alone.

The Raman spectroscopy has allowed us to probe relatively

small content of **CTC** in the host **8-PNP-O12** and obtain a reliable confirmation of the results which we have previously seen in the optical spectra. More importantly, it has provided us a solid proof of the predicted geometry by observation of the previously inactive vibrational bands. This allows us to propose the Raman spectroscopy as a valid tool alongside with IR spectroscopy to quantitatively estimate the amount of charge transfer. It is proposed that the molecular symmetry change upon the formation of **CTC** deserves a more in-depth inspection, since it may result in a significant change of the vibrational signature expressed by the apparition or by significant intensity change of the vibrational modes of the **CTC**. The results of vibrational spectroscopy have also confirmed that the **CTC** is not dependent on the mesophase nature and is thoroughly stable up to isotropic phase.

This observation has enabled us to use the TOF technique to find the bulk hole mobility in the mesophase. It is found that despite the stability of **CTC** remains high across both mesophases, the **CTC** itself has some effects on the mesophase structure. The hole mobility in each mesophase appears to increase with temperature, meaning that some charge trapping takes place in both mesophases. It is proposed that **CTC** is somehow able to disrupt the ordered layered structure of smectic mesophases, thus inducing some structural defects which may act as traps. In the Sm_A mesophase, whose order is inherently weaker compared to the Sm_B, the structural defects seem to provoke more severe charge carrier trapping, which explains why the hole mobility is decreasing proportionally to the introduction of the **F_4TCNQ**. It is also possible to suggest that the short-scale order of the Sm_A mesophase is more "vulnerable" to the disorder-inducing impurities than that of the Sm_B mesophase, as the resulting from doping charge carrier density increase is not able to compete with introduced traps. Thus, for the more ordered Sm_B mesophase, the role of structural defects may be partially negated by sufficient overlap of the dopant site potentials resulting from a more homogeneous **CTC** distribution in the layer, or trap filling by increased carrier density, which results in improvement of the hole mobility of the composites compared with that of pristine **8-PNP-O12**. In order to gain more insight on the observed mobility behavior it is necessary to reliably estimate the carrier density in both mesophases, which may be proven a non-trivial task due to strong ionic current contribution occurring on DC measurements in Sm_A mesophase.

It is of interest to address the common assumption of matching the frontier orbital energy levels of electron donor and acceptor. Generally, it is proposed that for adequate doping results the LUMO of the acceptor should be as close as possible to the HOMO of the donor to ensure efficient electron transfer. In this work we have showed that despite very close energy levels (less than 0.2 eV offset for **8-PNP-O12** and **F_4TCNQ** as opposed to 0.06 eV offset between 4T and **F_4TCNQ**[50]) the charge transfer amount is not strictly proportional to the value of the LUMO of the electron acceptor. We connect this behaviour to steric effects induced by the geometry of the pure **8-PNP-O12**. Relatively large dihedral angle (141.57°) between phenyl and naphthalene rings obstructs the access for one wing of the **F_4TCNQ**, which prevents it from being parallel to the molecule of **8-PNP-O12**. The result of this is the incomplete participation of electron-deficient nitrile groups on one wing of the **F_4TCNQ**, which is reflected in the asymmetric hybridization observed on the Figure 6, a. This asymmetry may also explain the results we have observed in the Raman spectra.

The main goal of our work is to postulate the necessity of scrupulous research of factors which reflect the influence of geometry on the efficiency of molecular doping. This underlines the importance of the term "molecular" in this process: (i) choice of the electron donor-acceptor system should be based not only on frontier molecular orbital energy levels, but also on the individual geometry; (ii) the result of donor-acceptor interaction in case of partial charge transfer (**CTC** formation) should be regarded as a unique supramolecular entity in order to predict its properties; (iii) careful attention should be addressed to the application of vibrational spectroscopy, as it is largely influenced by the molecular symmetry; (iv) the nature of change in the charge carrier transport should be properly inspected: the carrier mobility measurement should be accompanied by carrier density estimation in order to obtain the comprehensive picture.

Conflicts of interest

The authors declare that there is no conflict of interest regarding the publication of this article.

Acknowledgements

Kondratenko Kirill would like to thank Région Hauts-de-France for financial support. The authors gratefully acknowledge the use of facilities and instrumentation supported by the Soft Materials Research Center under NSF MRSEC Grant DMR-1420736.

Notes and references

1 J.-f. Chang, B. Sun, D. W. Breiby and M. M. Nielsen, *Chem. Mater.*, 2004, **16**, 4772–4776.
2 D. Braga and G. Horowitz, *Advanced Materials*, 2009, **21**, 1473–1486.
3 M. Pfeiffer, K. Leo, X. Zhou, J. S. Huang, M. Hofmann, A. Werner and J. Blochwitz-Nimoth, *Organic Electronics: physics, materials, applications*, 2003, **4**, 89–103.
4 H. Ebata, T. Izawa, E. Miyazaki, K. Takimiya, M. Ikeda, H. Kuwabara and T. Yui, *Journal of the American Chemical Society*, 2007, **129**, 15732–15733.
5 K. Walzer, B. Männig, M. Pfeiffer and K. Leo, *Chemical Reviews*, 2007, **107**, 1233–1271.
6 P. Pingel and D. Neher, *Physical Review B - Condensed Matter and Materials Physics*, 2013, **87**, 1–9.
7 G. Heimel, I. Salzmann and N. Koch, *AIP Conference Proceedings*, 2012, **1456**, 148–156.
8 B. Lüssem, M. Riede and K. Leo, *Physica Status Solidi (A) Applications and Materials Science*, 2013, **210**, 9–43.
9 W. Brütting, in *Physics of Organic Semiconductors*, Wiley-VCH Verlag GmbH & Co. KGaA, Weinheim, FRG, 2006, pp. 1–14.
10 F. Beniere, S. Haridoss, J. Louboutin, M. Aldissi and J. Fabre, *Journal of Physics and Chemistry of Solids*, 1981, **42**, 649–654.
11 P. Pingel, R. Schwarzl and D. Neher, *Appl. Phys. Lett.*, 2012, **100**, 143303.

12 C.-L. Fan, W.-C. Lin, H.-S. Chang, Y.-Z. Lin and B.-R. Huang, *Materials*, 2016, **9**, 46.

13 M. Pfeiffer, A. Beyer, B. Plönnigs, A. Nollau, T. Fritz, K. Leo, D. Schlettwein, S. Hiller and D. Wöhrle, *Solar Energy Materials and Solar Cells*, 2000, **63**, 83–99.

14 I. Avilov, V. Geskin and J. Cornil, *Advanced Functional Materials*, 2009, **19**, 624–633.

15 M. Bajpai, R. Srivastava, R. Dhar, R. S. Tiwari and S. Chand, *RSC Adv.*, 2014, **4**, 47899–47905.

16 I. Salzmann, G. Heimel, S. Duhm, M. Oehzelt, P. Pingel, B. M. George, A. Schnegg, K. Lips, R. P. Blum, A. Vollmer and N. Koch, *Physical Review Letters*, 2012, **108**, 1–5.

17 R. Kroon, D. Kiefer, D. Stegerer, L. Yu, M. Sommer and C. Müller, *Advanced Materials*, 2017, **29**, 1700930.

18 R. Mulliken and W. B. Person, *Annu. Rev. Phys. Chem*, 1962, **13**, 107–126.

19 B. Lussem, M. L. Tietze, H. Kleemann, C. Hossbach, J. W. Bartha, A. Zakhidov, K. Leo, B. Lüssem, M. L. Tietze, H. Kleemann, C. Hoßbach, J. W. Bartha, A. Zakhidov and K. Leo, *Nature Communications*, 2013, **4**, 1–6.

20 B. Xu, S. A. Gopalan, A. I. Gopalan, N. Muthuchamy, K. P. Lee, J. S. Lee, Y. Jiang, S. W. Lee, S. W. Kim, J. S. Kim, H. M. Jeong, J. B. Kwon, J. H. Bae and S. W. Kang, *Scientific Reports*, 2017, **7**, 1–12.

21 C. Liu, Z. Li, Z. Zhang, X. Zhang, L. Shen, W. Guo, L. Zhang, Y. Long and S. Ruan, *Phys. Chem. Chem. Phys.*, 2017, **19**, 245–250.

22 R. Sato, M. Dogishi, T. Higashino, T. Kadoya, T. Kawamoto and T. Mori, *Journal of Physical Chemistry C*, 2017, **121**, 6561–6568.

23 C. Ouyang, Y. Guo, H. Liu, Y. Zhao, G. Li, Y. Li, Y. Song and Y. Li, *Journal of Physical Chemistry C*, 2009, **113**, 7044–7051.

24 K. Xiao, A. J. Rondinone, A. A. Puretzky, I. N. Ivanov, S. T. Retterer and D. B. Geohegan, *Chemistry of Materials*, 2009, **21**, 4275–4281.

25 Goudappagouda, S. Chithiravel, K. Krishnamoorthy, S. W. Gosavi and S. Santhosh Babu, *Chemical Communications*, 2015, **51**, 10439–10442.

26 A. K. Thomas, R. Johnson, B. W. Stein, M. L. Kirk, H. Guo and J. K. Grey, *Journal of Physical Chemistry C*, 2017, **121**, 23817–23826.

27 S. V. Bhosale, M. A. Kobaisi, R. S. Bhosale, M. E. El-Khouly, D. D. La, S. D. Padghan, S. V. Bhosale, L. A. Jones, F. Antolasic and S. Fukuzumi, *Scientific Reports*, 2017, **7**, 1–11.

28 V. Coropceanu, J. Cornil, D. A. da Silva Filho, Y. Olivier, R. Silbey and J. L. Brédas, *Chemical Reviews*, 2007, **107**, 926–952.

29 F. Closs, K. Siemensmeyer, T. Frey and D. Funhoff, *Liquid Crystals*, 1993, **14**, 629–634.

30 B. A. Gregg and R. A. Cormier, *Journal of the American Chemical Society*, 2001, **123**, 7959–7960.

31 A. A. Khan, G. Rughoobur, M. A. Kamarudin, A. Sepe, J. A. Dolan, A. J. Flewitt, M. M. Qasim and T. D. Wilkinson, *Organic Electronics: physics, materials, applications*, 2016, **36**, 35–44.

32 M. Funahashi, *Materials Chemistry Frontiers*, 2017, **1**, 1137–1146.

33 N. Boden, R. J. Bushby and J. Clements, *The Journal of Chemical Physics*, 1993, **98**, 5920–5931.

34 M. Funahashi and J.-i. Hanna, *Applied Physics Letters*, 1997, **71**, 602–604.

35 N. Yoshimoto and J.-i. Hanna, *Journal of Materials Chemistry*, 2003, **13**, 1004–1010.

36 H. Iino and J. I. Hanna, *Journal of Physical Chemistry B*, 2005, **109**, 22120–22125.

37 T. Toda, J.-i. Hanna and T. Tani, *Journal of Applied Physics*, 2007, **101**, 024505.

38 S. Paul, B. Ellman, S. Tripathi and R. J. Twieg, *Journal of Applied Physics*, 2015, **118**, 135702.

39 Y.-F. Wang, H. Iino and J.-i. Hanna, *Soft Matter*, 2017, **13**, 6499–6505.

40 A. I. Baise, I. Teucher and M. M. Labes, *Applied Physics Letters*, 1972, **21**, 142–143.

41 H. Moritake, K. Toda, F. V. Podgornov, E. P. Pozhidaev and W. Haase, *Japanese Journal of Applied Physics, Part 1: Regular Papers and Short Notes and Review Papers*, 2006, **45**, 7538–7542.

42 M. J. Frisch, G. W. Trucks, H. B. Schlegel, G. E. Scuseria, M. A. Robb, J. R. Cheeseman, G. Scalmani, G. V. Barone, A. Petersson, H. Nakatsuji, X. Li, M. Caricato, A. V. Marenich, J. Bloino, B. G. Janesko, R. Gomperts, B. Mennucci, H. P. Hratchian, J. V. Ortiz, A. F. Izmaylov, J. L. Sonnenberg, D. Williams-Young, F. Ding, F. Lipparini, F. Egidi, J. Goings, B. Peng, A. Petrone, T. Henderson, D. Ranasinghe, V. G. Zakrzewski, J. Gao, N. Rega, G. Zheng, W. Liang, M. Hada, M. Ehara, K. Toyota, R. Fukuda, J. Hasegawa, M. Ishida, T. Nakajima, Y. Honda, O. Kitao, H. Nakai, T. Vreven, K. Throssell, J. A. Montgomery, J. E. Peralta, F. Ogliaro, M. J. Bearpark, J. J. Heyd, E. N. Brothers, K. N. Kudin, V. N. Staroverov, T. A. Keith, R. Kobayashi, J. Normand, K. Raghavachari, A. P. Rendell, J. C. Burant, S. S. Iyengar, J. Tomasi, M. Cossi, J. M. Millam, M. Klene, C. Adamo, R. Cammi, J. W. Ochterski, R. L. Martin, K. Morokuma, O. Farkas, J. B. Foresman and D. J. Fox, *Gaussian 16, Revision A.03*, 2016.

43 A. Kokil, K. Yang and J. Kumar, *Journal of Polymer Science, Part B: Polymer Physics*, 2012, **50**, 1130–1144.

44 K. Sengupta, V. A. Raghunathan and J. Katsaras, *Physical Review E - Statistical Physics, Plasmas, Fluids, and Related Interdisciplinary Topics*, 2003, **68**, 12.

45 K. Liu, D. Chen, A. Marcozzi, L. Zheng, J. Su, D. Pesce, W. Zajaczkowski, A. Kolbe, W. Pisula, K. Müllen, N. A. Clark and A. Herrmann, *Proceedings of the National Academy of Sciences*, 2014, **111**, 18596–18600.

46 N. Vaupotič, M. Čepič, J. Mieczkowski, D. Pociecha, E. Gorecka and K. Gomola, *Journal of Materials Chemistry*, 2008, **18**, 3044.

47 C. Zhang, N. Diorio, S. Radhika, B. K. Sadashiva, S. N. Sprunt and A. Jákli, *Liquid Crystals*, 2012, **39**, 1149–1157.

48 D. P. Singh, R. Visvanathan, A. E. Duncan, B. Duponchel, Y. Boussoualem, S. Kumar, N. A. Clark, J.-F. Blach, R. Douali

and A. Daoudi, *Liquid Crystals*, 2018, **00**, 1–10.
49 D. Tadaki, T. Ma, J. Zhang, S. Iino, A. Hirano-Iwata, Y. Kimura and M. Niwano, *Japanese Journal of Applied Physics*, 2015, **54**, 091602.
50 H. Méndez, G. Heimel, S. Winkler, J. Frisch, A. Opitz, K. Sauer, B. Wegner, M. Oehzelt, C. Röthel, S. Duhm, D. Többens, N. Koch and I. Salzmann, *Nature Communications*, 2015, **6**, 8560.
51 L. Zhu, E. G. Kim, Y. Yi and J. L. Brédas, *Chemistry of Materials*, 2011, **23**, 5149–5159.
52 J. H. Lee, D. S. Leem, H. J. Kim and J. J. Kim, *Applied Physics Letters*, 2009, **94**, 19–22.
53 D. A. Dixon, J. C. Calabrese and J. S. Miller, *The Journal of Physical Chemistry*, 1989, **93**, 2284–2291.
54 D. T. Duong, C. Wang, E. Antono, M. F. Toney and A. Salleo, *Organic Electronics: physics, materials, applications*, 2013, **14**, 1330–1336.
55 S. G. Liu, G. Sui, R. A. Cormier, R. M. Leblanc and B. A. Gregg, *Journal of Physical Chemistry B*, 2002, **106**, 1307–1315.
56 B. A. Gregg and M. E. Kose, *Chemistry of Materials*, 2008, **20**, 5235–5239.
57 M. Meneghetti and C. Pecile, *The Journal of Chemical Physics*, 1986, **84**, 4149–4162.
58 D. Di Nuzzo, C. Fontanesi, R. Jones, S. Allard, I. Dumsch, U. Scherf, E. Von Hauff, S. Schumacher and E. Da Como, *Nature Communications*, 2015, **6**, 1–8.
59 J. S. Kim, S. K. Lee, H. J. Lee and D. Y. Noh, *Bulletin of the Korean Chemical Society*, 2010, **31**, 1415–1418.
60 J. Gao, J. D. Roehling, Y. Li, H. Guo, A. J. Moulé and J. K. Grey, *Journal of Materials Chemistry C*, 2013, **1**, 5638.
61 S. Kudoh, M. Takayanagi and M. Nakata, *Chemical Physics Letters*, 2000, **322**, 363–370.
62 T. Osaki and E. Soeijima, *Res. Bull. Fukoka Inst. Tech*, 2010, **42**, 129–134.
63 E. Kampar and O. Neilands, *Russian Chemical Reviews*, 1986, **55**, 334–342.
64 R. J. Bushby and O. R. Lozman, *Current Opinion in Solid State and Materials Science*, 2002, **6**, 569–578.
65 K. Hudson, B. Ellman, V. Gettwert, Y. Getmanenko and R. J. Twieg, *Applied Physics Letters*, 2005, **87**, 1–3.
66 T. Wöhrle, I. Wurzbach, J. Kirres, A. Kostidou, N. Kapernaum, J. Litterscheidt, J. C. Haenle, P. Staffeld, A. Baro, F. Giesselmann and S. Laschat, *Chemical Reviews*, 2016, **116**, 1139–1241.
67 K. P. Gan, M. Yoshio, Y. Sugihara and T. Kato, *Chemical Science*, 2018, **9**, 576–585.
68 K. Kondratenko, D. Singh, Y. Boussoualem, R. Douali, C. Legrand and A. Daoudi, *Journal of Molecular Liquids*, 2019, **276**, 27–31.
69 I. Shiyanovskaya, K. D. Singer, R. J. Twieg, L. Sukhomlinova and V. Gettwert, *Physical Review E - Statistical, Nonlinear, and Soft Matter Physics*, 2002, **65**, 1–13.
70 G. Zuo, Z. Li, O. Andersson, H. Abdalla, E. Wang and M. Kemerink, *Journal of Physical Chemistry C*, 2017, **121**, 7767–7775.
71 J.-i. Hanna, A. Ohno and H. Iino, *Thin Solid Films*, 2014, **554**, 58–63.
72 M. Funahashi and J. I. Hanna, *Chemical Physics Letters*, 2004, **397**, 319–323.
73 S. G. Chen, P. Stradins and B. A. Gregg, *Journal of Physical Chemistry B*, 2005, **109**, 13451–13460.
74 I. V. Arkhipov, P. Heremans, E. V. Emelianova, G. J. Adriaenssens and H. Bässler, *Journal of Physics Condensed Matter*, 2002, **14**, 9899–9911.
75 C. C. Huang, in *Handbook of Liquid Crystals*, Wiley-VCH Verlag GmbH, Weinheim, Germany, 1998, pp. 441–469.

Novel composites of mesogenic organic semiconductor and electron acceptor exhibit charge transport dynamics strongly correlated to the liquid crystal order.